BUTTERWORTH HEINEMANN

Buoyancy effects on the wake behind a heated obstacle immersed in a turbulent boundary layer

Y. S. Mori, K. Hishida, and M. Maeda
Department of Mechanical Engineering, Keio University, Yokohama, Japan

The effects of buoyancy on the wake behind a two-dimensional (2-D) heated obstacle immersed in a turbulent boundary layer have been examined both experimentally and numerically in an effort to understand the thermal release over complex terrain in an idealized environmental flow. Emphasis was placed on clarifying the modification of the production agencies of the turbulence kinetic energy, resulting both from the direct and indirect buoyant contributions. Buoyancy altered the mean velocity field along the extent of the recirculating region and resulted in a reduction of the turbulent kinetic energy in the vicinity of the obstacle and, through an enhanced shear production, a growth downstream. Buoyant production of turbulent kinetic energy dominated the shear production outside the recirculating region, where the temperature variance was significant. Numerical predictions obtained by a recent buoyancy-extended k-ε model were found to give the analogous properties of buoyant motion appearing in the experimental results.

Keywords: buoyancy effects; forced convection; recirculating flow; laser Doppler anemometer measurement; two-equation model

Introduction

The flow field in the atmospheric boundary layer has been of primary concern in environmental researches (Turner 1973), with recent emphasis placed on the thermal accumulation around the industrial areas where the complex topography and the buoyancy introduced by thermal release interact. Such circumstances arise when air flow over a heated region forms the wake in which buoyancy affects the fluid motion and the transport process. Effects of the buoyancy on the flow field can be distinguished in two different types (Tennekes and Lumley 1973). Time-averaged buoyancy affects the mean velocity field and this, in turn, modifies the shear production of turbulent quantities. Meanwhile, fluctuations act directly as a source or sink on the production of turbulent quantities. Buoyancy, therefore, modifies the flow characteristics providing particular features both of mean velocity field and turbulence field. However, it is not clear which of these two mechanisms dominates, especially in complicated flows accompanied both with topographic and thermal conditions. Then, numerical approaches have a potential to clarify the reliable capture of the buoyancy effects in question. At present, although the second moment closure model has been developed by Launder (1975) and Gibson et al. (1978), the k-ε model with a simple buoyancy extended form seems to be most suitable for practical flow problems (Markatos et al. 1982; Demuren et al. 1987).

The objective of the present study is to clarify both experimentally and numerically the buoyancy effects on the wake characteristics behind a heated two-dimensional (2-D) obstacle placed in a turbulent boundary layer, a flow meant to approximate those observed in the atmosphere. Numerical simulations are performed by a k-ε model that employs an algebraic expression for the buoyant production term (Launder 1989) in the k-equation. In particular, the manners in which buoyancy acts directly or indirectly on the production agencies of turbulence kinetic energy are clarified together with experimental results.

Address reprint requests to Prof. Koichi Hishida, Department of Mechanical Engineering, Keio University, 3-14-1 Hiyoshi, Kohoku, Yokohama 223, Japan.

Received 27 September 1994; accepted 4 April 1995

Experimental arrangement

Flow system

A schematic view of the flow field is shown in Figure 1. Experiments were conducted in an open-air wind tunnel whose longitudinal section is shown in Figure 2. The test section was a rectangular channel with dimensions of 1500 mm, 240 mm, and 250 mm in the streamwise, transverse, and spanwise directions, respectively. The test section walls were made of transparent acrylic to enable laser Doppler anemometer (LDA) measurements at any location along the channel. Two-dimensional flow in the test section was achieved in the range of $z/h = \pm 3$. To simulate the atmospheric boundary-layer profile in the wind tunnel, a shear generator that was composed of the round cross-sectioned rods of 2.0-mm diameter with variable spacing was used, with which the relatively thicker boundary layer than that developed over the flat plate could be formed along the test section. A boundary-layer profile was determined by changing the allocation of each rod. The shear generator was located 550-mm upstream from the obstacle position, far enough to smooth the rough boundary-layer profile due to the wake interference behind the rods.

A square cross-sectioned obstacle ($30 \times 30 \times 250$-mm) consisted of a copper body with a highly polished surface and a

Int. J. Heat and Fluid Flow 16: 405–416, 1995

655 Avenue of the Americas, New York, NY 10010

0142-727X/95/$10.00
SSDI 0142-727X(95)00055-U

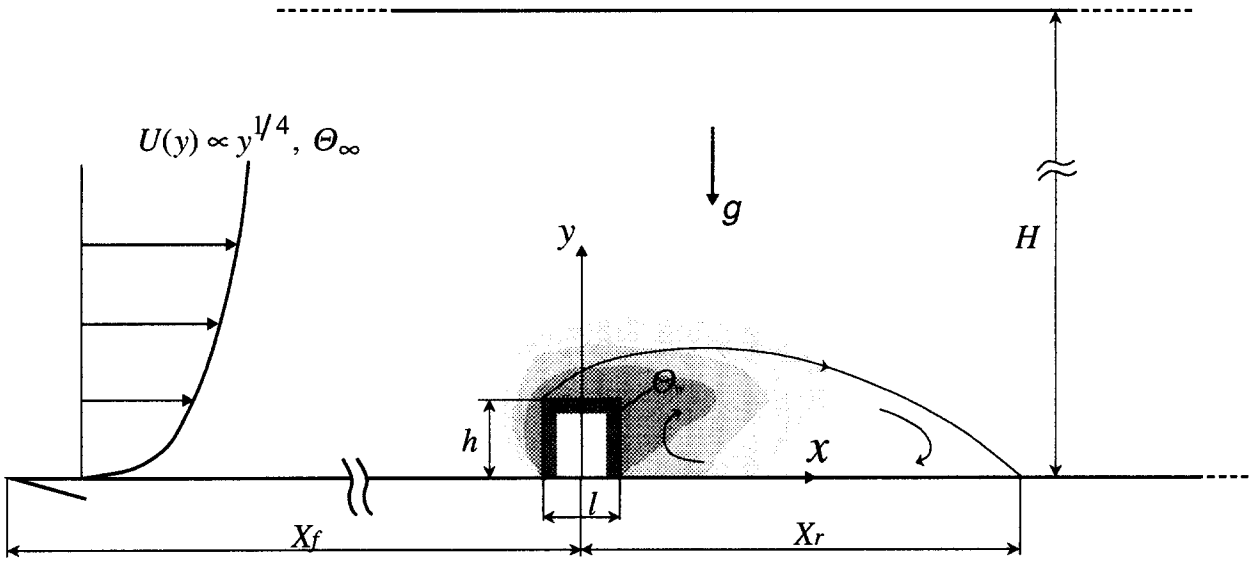

Figure 1 A schematic view of flow field

high-power cartridge heater inside. The obstacle was mounted firmly on a well-insulated fine ceramic wall (20-mm thickness) to minimize the conductive heat loss. In addition, both ends of the obstacle were covered with the asbestos walls (15-mm thickness). The conductive heat loss to the ambient wall was estimated less than 10% of the total heat input, and the radiated heat loss was

Notation

C_μ, $C_{\varepsilon 1}$, $C_{\varepsilon 2}$, $C_{\varepsilon 3}$	model constants for velocity field
$C_{\theta 1}$, $C_{\theta 2}$, $C_{\theta 3}$	model constants for algebraic flux model of $\overline{u_i\theta}$
C_P	specific heat capacity at constant pressure
g_i	gravitational acceleration, $(0, -g, 0)$
G_k	buoyant production term in k-equation
H	height of test section
h	obstacle height
k	turbulence kinetic energy
L	turbulence length scale
l	obstacle width
P	pressure
P_k	shear production term in k-equation
P_θ	production term in $\overline{\theta^2}$-equation
Pr	Prandtl number, ν/α
Pr_t	turbulent Prandtl number, ν_t/α_t
Q_w	wall heat flux
R	ratio of mechanical-to-thermal time scale of turbulence, $(\overline{\theta^2}/2\varepsilon_\theta)/(k/\varepsilon)$
Re_h	Reynolds number based on obstacle height h and mean velocity U_h measured at the obstacle height $y/h = 1$ at $x/h = 0$, $U_h h/\nu$
Ri	over-all Richardson number based on temperature difference between wall temperature Θ_w and free-stream temperature Θ_∞, $g\beta h(\Theta_\infty - \Theta_w)/U_h^2$
R_f	flux Richardson number, $-G_k/P_k$
S	strain parameter in P_k
u_i	fluctuating velocity
u, v, w	streamwise, vertical, and spanwise fluctuating velocities
U_i	mean velocity
U, V	streamwise and vertical mean velocities
$\overline{u_i u_j}$	Reynolds stress tensor
$\overline{u_i\theta}$	thermometric turbulent heat flux tensor
x_i	coordinate in tensor notation
x, y, z	streamwise, transverse, and spanwise coordinates
X_f	length from the leading edge to the obstacle location
X_r	reattachment length

Greek

α, α_t	molecular and turbulent thermal diffusivity
β	coefficient of volumetric expansion
δ	boundary-layer thickness
ε, ε_θ	dissipation rate of k and $\overline{\theta^2}/2$
$\overline{\theta^2}$	temperature variance
Θ	mean temperature
ν, ν_t	molecular and turbulent kinematic viscosity
ρ	fluid density
σ_k, σ_ε, σ_θ	model constants for turbulent diffusion
ψ	stream function
Ω	vorticity parameter in P_k

Subscripts

i, j, k	integers used in index notation relation
w	wall condition
∞	free-stream condition

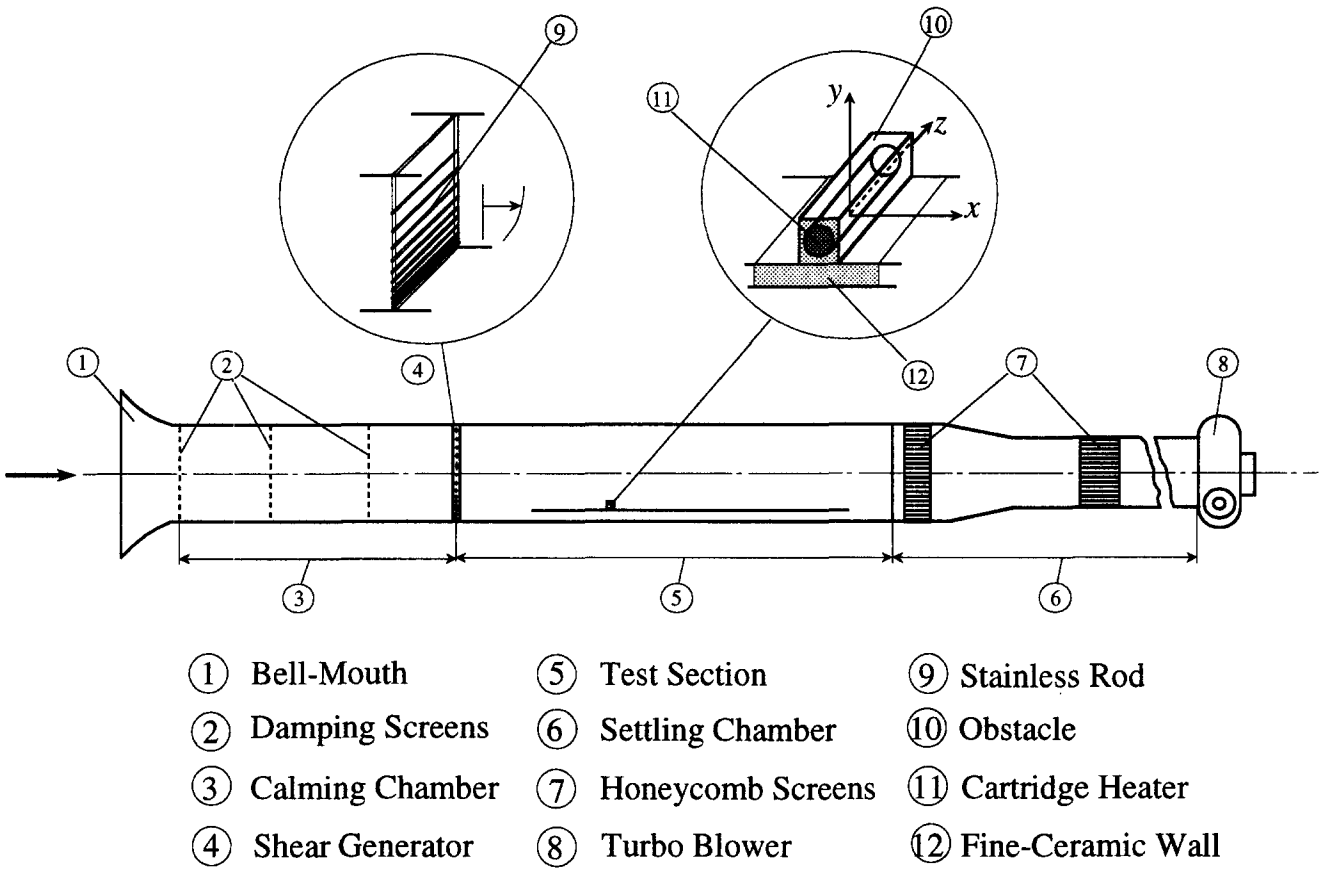

Figure 2 Experimental flow system

calculated to be less than 3%. The wall temperature was monitored by Ar-Cr thermocouples of 0.1-mm diameter, which were embedded on the face of the obstacle. The coordinate system, originating in the bottom of the obstacle midpoint, was an orthogonal one with x, y, and z in streamwise, transverse, and spanwise directions, respectively. The geometric parameters are summarized in Table 1.

Measuring system

A two-beam, one-component, and back-scattering LDA system whose light source was He-Ne laser of 10 mW was used for velocity measurements. The measurement volume of LDA was $86 \times 86 \times 646[\mu m]$, which made it possible to perform the measurement as close to the wall as possible: at 1 mm from the wall. A single-mode polarization-preserving fiber was used to transmit the incident light beam to the probe head, while double Bragg cells were employed for frequency shifting to measure flow reversals. For signal processing, a counter (TSI-type 1980B, 500-MHz sampling clock) was employed. A fiber-based transmitting unit was fixed at a three-dimensional (3-D) traversing unit that provided 0.02 mm positional accuracy. A mist of salad oil of 1-μm diameter was mixed with the operational fluid as the tracer particles at the inlet. The sampling number for the particles was 3000 for each point, which was considered to be large enough to minimize the statistical bias error, even at any location where a highly turbulent flow was observed.

Table 1 Experimental conditions

Obstacle height	h, m	0.03
Obstacle width	l, m	0.03
Blockage ratio	H/h	8.0
Length from leading edge to obstacle	X_f, m	0.25
Free-stream velocity	U_∞, m/s	1.00
Reference velocity	U_h, m/s	0.69
Reynolds number	$Re_h = U_h h/\nu$	1320
Boundary-layer thickness	δ, m	0.12
Free-stream temperature	Θ_∞, K	290–293
Obstacle wall temperature	Θ_w, K	740
Overall Richardson number	$Ri = g\beta h(\Theta_\infty - \Theta_w)/U_h^2$	−0.9

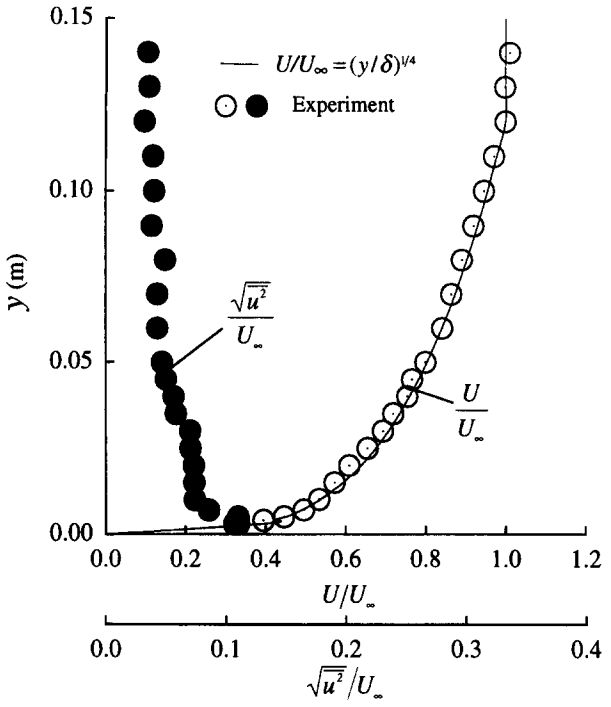

Figure 3 Inlet profiles of mean and fluctuating velocities ($x/h = -7$, without an obstacle)

Mean temperatures were measured by standard thermocouples (Cu-Co of 0.1-mm diameter). The voltage at the measurement junction was amplified and digitized by a 100-KHz, 12-bit A/D converter, and averages were calculated on a microcomputer. For temperature variance measurements, a resistance thermometer of 5-μm tungsten (I-probe) wire was used. The measurement was performed by using a thermobridge providing constant current (1 mA) with the cold wire. The evaluated time constant of the resistance thermometer including a support rod was approximately 5.0 ms, which was sufficient for the dominant time scale along the separated shear layer (Tennekes and Lumley 1973). The detected imbalance in resistance thermometer was transformed to a voltage output by thermobridge (KANOMAX 1010 sensitivity −1.6 mV/°C) via an amplifier and band-pass filter and was quantified by an rms meter with 4 1/2 digit accuracy.

Experimental conditions

The boundary-layer profile created by the shear generator is shown in Figure 3. The inlet profile of the boundary layer was defined at $x/h = -7$ for the condition when the obstacle was removed. Taking the normalizing mean velocity U_∞ at the center line of test section $y/h = 4$, the resultant profile of an approaching boundary layer was approximately described by the power-law relation of $U/U_\infty = (y/\delta)^{1/4}$. A boundary-layer thickness δ was set to be about 4 × the obstacle height h. As a result of highly sheared mean flow, relatively large magnitude of turbulence intensities were obtained, ranging from 4% to 12%, as also seen in Figure 3.

The experiments were conducted at $\mathrm{Re}_h = 1320$ based on the obstacle height h and mean velocity U_h that was measured at the height of obstacle level $y/h = 1$ at $x/h = 0$ without placing the obstacle. The velocity measurements were performed in x–y plane ranging from $x/h = 0$ to $x/h = 10.5$ downstream in every $x/h = 1.5$ step. The overall Richardson number (R_i) was employed as the parameter to represent the buoyancy effects on the flow domain. The overall Richardson number was set at $R_i = -0.90$ based on the wall temperature obtained from the arithmetic average value of local 15 points over the obstacle surface at $z/h = 0$.

Measuring uncertainty within 95% confidence interval for each value was obtained at $x = 90$ mm and $y = 40$ mm as follows; for the mean velocity U/U_h and V/U_h uncertainties were ± 0.029 and ± 0.035 respectively; for the turbulence kinetic energy k/U_h^2 the uncertainty was ± 0.033. The uncertainties of mean temperature $(\Theta - \Theta_\infty)/(\Theta_w - \Theta_\infty)$ and temperature variance $\overline{\theta^2}/(\Theta_w - \Theta_\infty)^2$ were ± 0.051 and ± 0.081, respectively.

Numerical procedure

The governing equations with the evolution both of turbulence energy production and of buoyancy extension are given below.

Governing equations

Because the flow field is steady-state, incompressible, and 2-D turbulent flow, the governing Reynolds averaged conservation equations for mass, momentum, and energy are, respectively, written as follows:

$$\frac{\partial}{\partial x_i}(\rho U_i) = 0 \tag{1}$$

$$\frac{\partial}{\partial x_j}(\rho U_j U_i) = -\frac{\partial}{\partial x_i}\left(P + \frac{2}{3}\rho k\right) + \frac{\partial}{\partial x_j}\left[\rho\nu\left(\frac{\partial U_i}{\partial x_j} + \frac{\partial U_j}{\partial x_i}\right) - \rho\overline{u_i u_j}\right] + g_i(\rho - \rho_\infty) \tag{2}$$

$$\frac{\partial}{\partial x_j}(\rho C_P U_j \Theta) = \frac{\partial}{\partial x_j}\left(\rho C_P \frac{\nu}{P_r}\frac{\partial \Theta}{\partial x_j} - \rho C_P \overline{u_j \theta}\right) \tag{3}$$

In Equations 2 and 3, the unknown correlations, Reynolds stresses, and thermometric turbulent heat fluxes are obtained via the eddy viscosity hypothesis for the moment and the heat,

$$\overline{u_i u_j} = -\nu_t\left(\frac{\partial U_i}{\partial x_j} + \frac{\partial U_j}{\partial x_i}\right) + \frac{2}{3}\delta_{ij}k \tag{4}$$

$$\overline{u_j \theta} = -\frac{\nu_t}{P_{r_t}} \cdot \frac{\partial \Theta}{\partial x_j} \tag{5}$$

In these equation, the Boussinesq approximation was not adopted for the treatment of density variation. The local density was assumed to be the function only of the local mean temperature (Demuren and Rodi 1987). In addition, the molecular viscosity was given by the Sutherland's formula (Davidson 1990).

It is well known that the standard production term of turbulence energy P_k gives the extremely large production at the front corner of the obstacle where a stagnation exists, resulting in the poor prediction of the flow characteristics near wake. To remove this unfavorable excessive production of k at the stagnation region, we adopted the modified model of P_k proposed by Kato and Launder (1993), which was coupled with the vorticity parameter Ω and dimensionless strain S, in place of the standard production term. In that study, the use of modified P_k was examined in the prediction of flow past a 2-D square cylinder, which made the predicted results of fluctuating energy, as well as of mean velocity, on the symmetric line even in near wake better than those done by using standard production term.

The buoyant production term G_k includes the thermometric turbulent heat flux $\overline{u_i\theta}$. The basis of the adopted model is an

Table 2 Constants in the turbulence model

C_μ	$C_{\varepsilon 1}$	$C_{\varepsilon 2}$	$C_{\varepsilon 3}$	σ_k	σ_ε	Pr_t	σ_θ	$C_{\theta 1}$	$C_{\theta 2}$	$C_{\theta 3}$	R
0.09	1.92	1.44	0 ($G_k<0$), 1 ($G_k>0$)	1.0	1.3	0.9	1.0	0.28	0.4	0.4	0.5

implicit algebraic flux modeling of $\overline{u_i\theta}$ (Launder 1989). This expression includes the fact that the turbulent heat flux in the vertical direction can be driven by the temperature variance $\overline{\theta^2}$ in the absence of mean temperature or velocity gradients. The equations for k and ε including buoyancy effects are, respectively, given as

$$\frac{\partial}{\partial x_j}(\rho U_j k) = \frac{\partial}{\partial x_j}\left\{\rho\left(\nu + \frac{\nu_t}{\sigma_k}\right)\frac{\partial k}{\partial x_j}\right\} + P_k + G_k - \rho\varepsilon \tag{6}$$

$$\frac{\partial}{\partial x_j}(\rho U_j \varepsilon) = \frac{\partial}{\partial x_j}\left\{\rho\left(\nu + \frac{\nu_t}{\sigma_\varepsilon}\right)\frac{\partial \varepsilon}{\partial x_j}\right\} + C_{\varepsilon 1}\frac{\varepsilon}{k}(P_k + C_{\varepsilon 3}G_k) - \rho C_{\varepsilon 2}\frac{\varepsilon^2}{k} \tag{7}$$

The modified P_k suggested by Kato and Launder (1993) is

$$P_k = \rho C_\mu \varepsilon S \Omega \tag{8}$$

where

$$S = \frac{k}{\varepsilon}\sqrt{\frac{1}{2}\left(\frac{\partial U_i}{\partial x_j} + \frac{\partial U_j}{\partial x_i}\right)^2} \tag{9}$$

$$\Omega = \frac{k}{\varepsilon}\sqrt{\frac{1}{2}\left(\frac{\partial U_i}{\partial x_j} - \frac{\partial U_j}{\partial x_i}\right)^2} \tag{10}$$

The thermometric turbulent heat flux $\overline{u_i\theta}$ in $G_k = -\rho g_i \beta \overline{u_i\theta}$ is

$$\overline{u_i\theta} = -C_{\theta 1}\frac{k}{\varepsilon}\left[\overline{u_i u_k}\frac{\partial \Theta}{\partial x_k} + (1-C_{\theta 2})\overline{u_k\theta}\frac{\partial U_i}{\partial x_k} + (1-C_{\theta 3})g_i\beta\overline{\theta^2}\right] \tag{11}$$

where the empirical constants proposed by Hanjalić and Vasić (1993) were adopted. The analogous transport equation to the turbulence kinetic energy k leads the transport equation of $\overline{\theta^2}$ (Corrsin 1951) as follows:

$$\frac{\partial}{\partial x_j}\left(\rho U_j\overline{\theta^2}\right) = \frac{\partial}{\partial x_j}\left\{\rho\left(\frac{\nu}{\mathrm{Pr}} + \frac{\nu_t}{\sigma_\theta}\right)\frac{\partial\overline{\theta^2}}{\partial x_j}\right\} - 2\rho\overline{u_i\theta}\frac{\partial\Theta}{\partial x_i} - 2\rho\varepsilon_\theta \tag{12}$$

Because the modeling of ε_θ must be undertaken, a local value of ε_θ is calculated from the algebraic expression associated with the time scale ratio R (Béguier et al. 1983). Then ε_θ is

$$\varepsilon_\theta \equiv \frac{\overline{\theta^2}}{2R}\cdot\frac{\varepsilon}{k} \tag{13}$$

The second moments in the production term were calculated from the eddy-viscosity expressions of Equations 4 and 5. A further constant $C_{\varepsilon 3}$ in ε-equation was adopted by the Viollet model (1987). The constant $C_{\varepsilon 3}$ should take the value of 1 when the buoyant production term G_k acts as a source ($G_k > 0$) of turbulence kinetic energy k, and the value of 0 is recommended for $C_{\varepsilon 3}$ in case the buoyant production term G_k acts as a sink ($G_k < 0$) of turbulence energy. A summary of other empirical constants is given in Table 2.

Boundary conditions are summarized in Table 3. Each quantity at the inlet plane was taken from the experimental data, while the dissipation rate ε was defined practically by relating the turbulence length scale L to the constant value after checking its suitability. Because the boundary layer profile was artificially developed by using the shear generator, the dissipation rate ε at the inlet was not derived from the usual assumption that the turbulence is in local equilibrium within the turbulent boundary layer. After running the calculation with some varieties of the inlet condition for ε, it was proved that the definition of ε described in Table 3 gave the best agreement with experimental results, in which the turbulence length scale L was a constant value of $4h$ instead of using the functionalized distribution of L.

At the first grid nodes adjacent to the solid wall, including those over the obstacle surface, the computations for the velocity field was specified according to the standard wall function approach. For the thermal condition on the solid wall except the surface of the heated obstacle, the adiabatic state was assumed, which fulfilled the conditions that the mean temperature gradient between the first grid node and the wall face, as well as the temperature variance gradient could be neglected. As for the thermal condition at the first grid nodes over the heated obstacle, instead of using the log-law relation for the mean temperature, the simplified expression that the wall heat flux can be described in terms of the gradient diffusion was applied, as indicated in Table 3. The thermometric heat flux $\overline{u_n\theta}$ at the first grid node

Table 3 Boundary conditions

Inlet	U, V, k: experiment, $3 = C_\mu^{3/4}k^{3/2}/L$ ($L = 4h$)
	$\Theta = \Theta_\infty$, $\overline{\theta^2} = 0$
Outlet	Neumann condition ($\partial/\partial n = 0$)
Solid wall	U, V, k, ε: standard wall function
	Θ, $\overline{\theta^2}$: $\partial\Theta/\partial n = \partial\overline{\theta^2}/\partial n = 0$ (adiabatic wall)
Wall of heated obstacle	U, V, k, ε: standard wall function (eddy viscosity for $-\overline{u_n\theta}$ in G_k)
	First grid node:
	Θ: $\dfrac{Q_w}{\rho C_p} = \overline{u_n\theta} - \dfrac{\nu}{P_r}\cdot\dfrac{\partial\Theta}{\partial n}$
	$\overline{\theta^2}$: $P_\theta = -2\rho\overline{u_n\theta}\dfrac{\partial\Theta}{\partial n}$ (eddy viscosity for $-\overline{u_n\theta}$)
	Wall surface:
	Θ_w: experiment, $\overline{\theta^2} = 0$
	n: normal to boundary

was calculated from the eddy-viscosity hypothesis only for the component expressed by the mean temperature gradient normal to the wall, and the measured values of the mean temperature on the heated wall were used to prescribe the boundary values over the surface of the obstacle.

Numerical calculations were carried out by means of a finite-volume solver based on the CAST code (Perić and Sheuerer 1989) that employs nonuniform grids and collocated variable arrangement with SIMPLE algorithm for the coupling of mean velocity and pressure fields (Obi and Perić 1991). The inlet section of the computational domain was located at $x/h = -3$ and the outlet at $x/h = 30$ far downstream from the reattachment point enough to exclude any effects of the reverse flow. The grid system was composed of 161×93 grid nodes. Figure 4 shows a part of computing mesh covering the section in the vicinity of the obstacle. In the y-direction, mesh generation adjacent to the top wall of the obstacle was set to be concentrated as done by Obi (1991), where the production of the turbulence quantities would take their maximum values due to the steeper gradient of mean velocity. The CAST code employs the flux-blending scheme as a discretization for the convective term (Khosla and Rubin 1974),

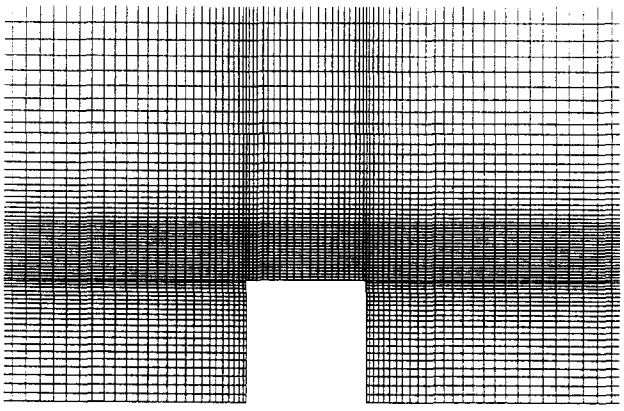

Figure 4 Computing mesh in the vicinity of the obstacle

which is the linear combination of the first-order upwind differential scheme and the second-order differential scheme to include both of their advantages that secure the steady state solution.

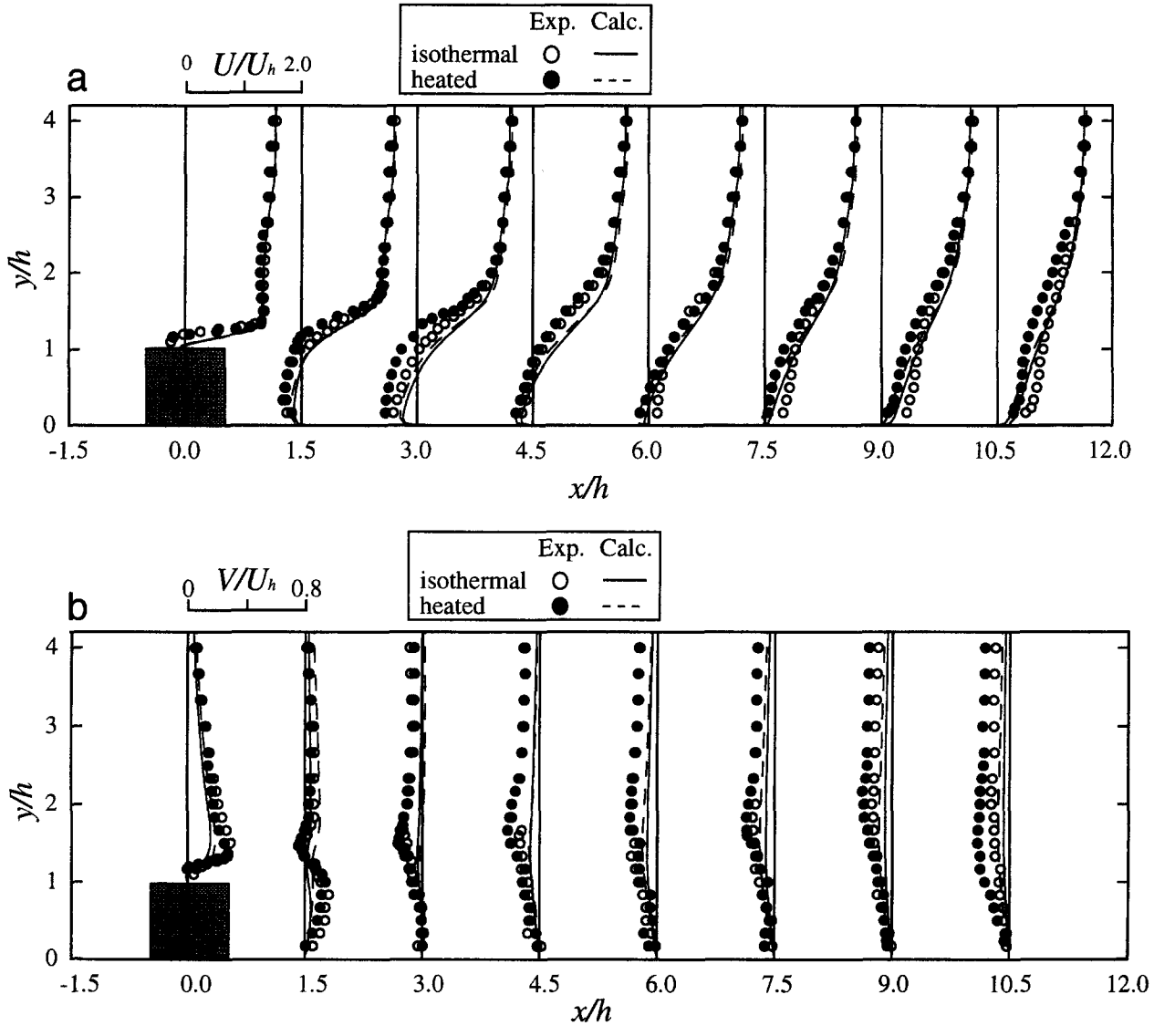

Figure 5 Experimental and calculated results of mean velocity profiles, (a) x-component, U/U_h; (b) y-component, V/U_h

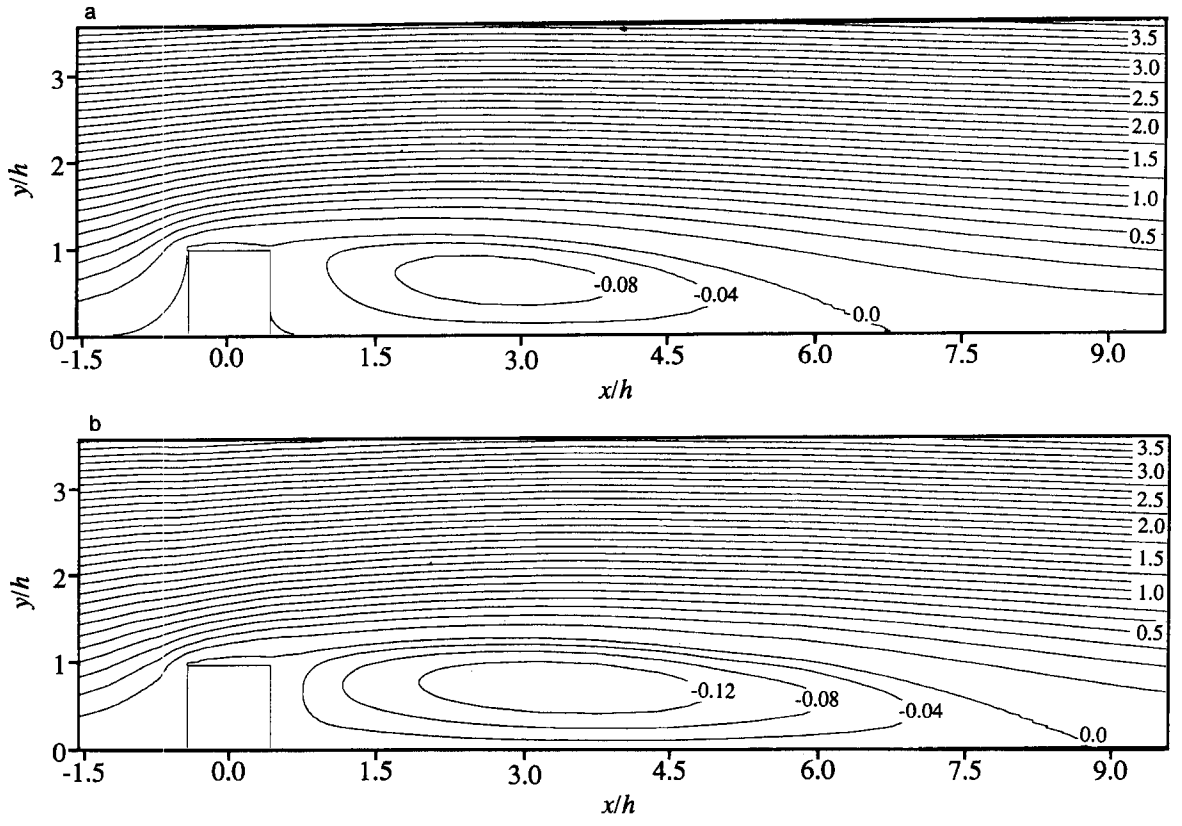

Figure 6 Calculated streamlines, $\rho\psi/\rho_\infty U_h h$; (a) isothermal flow; (b) heated flow

Results and discussion

Buoyancy effects on mean velocity field

The buoyancy effects on the mean velocity field observed in the experimental results are discussed with the aid of numerical results. The comparison of experimental and calculated results of mean velocity profiles are presented in Figures 5a and b. Both measured and calculated results are normalized by the measured reference velocity U_h. Figure 5a shows that the gradient of the shear flow in the heated result was steeper than that of the isothermal one in the range of $1 < y/h < 1.4$ at $x/h = 1.5$ and 3.0, and the region of negative mean velocity is apparently spread

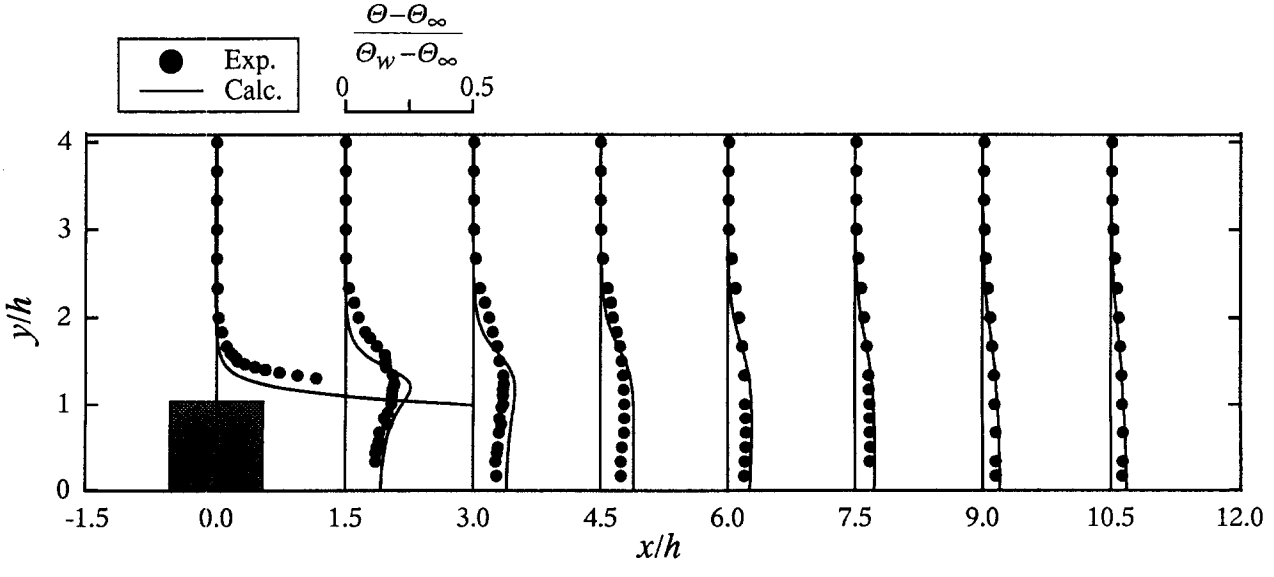

Figure 7 Experimental and calculated results of mean temperature profiles, $(\Theta - \Theta_\infty)/(\Theta_w - \Theta_\infty)$

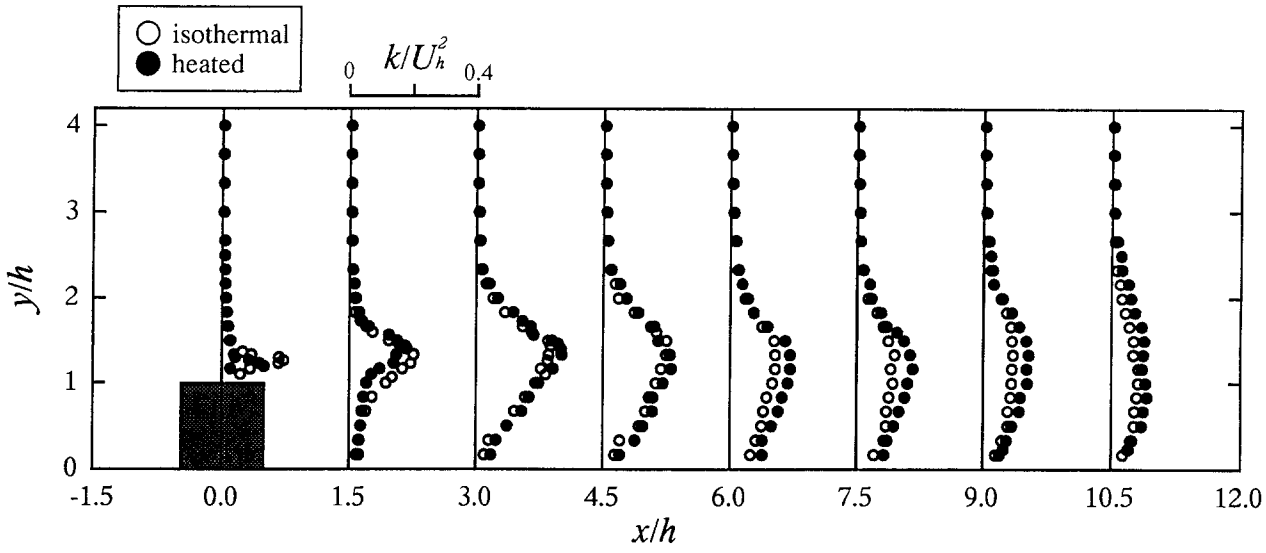

Figure 8 Experimental results of turbulence kinetic energy profiles, k/U_h^2

at $x/h = 3.0$. The reattachment length, one of the wake characteristics, Xr was extended from $Xr = 5.4h$ to $Xr = 6.7h$ in the measurement. After reattachment, the mean velocity profiles show a slower recovery than the isothermal one as a consequence having a longer reattachment length. Calculated results also show the same trend as that observed in the experimental results. The predicted reattachment lengths Xr were $7.0h$ for the isothermal condition and $8.4h$ for the heated condition. Seeing the profiles of vertical mean velocity in Figure 5b, the results of prediction failed to give a good agreement with experimental results, as are often the cases with those done using k-ε model. The extension of recirculating region causes a relatively larger value of descending flow in the range of $9.0 < x/h < 10.5$ as seen both in measured and calculated results.

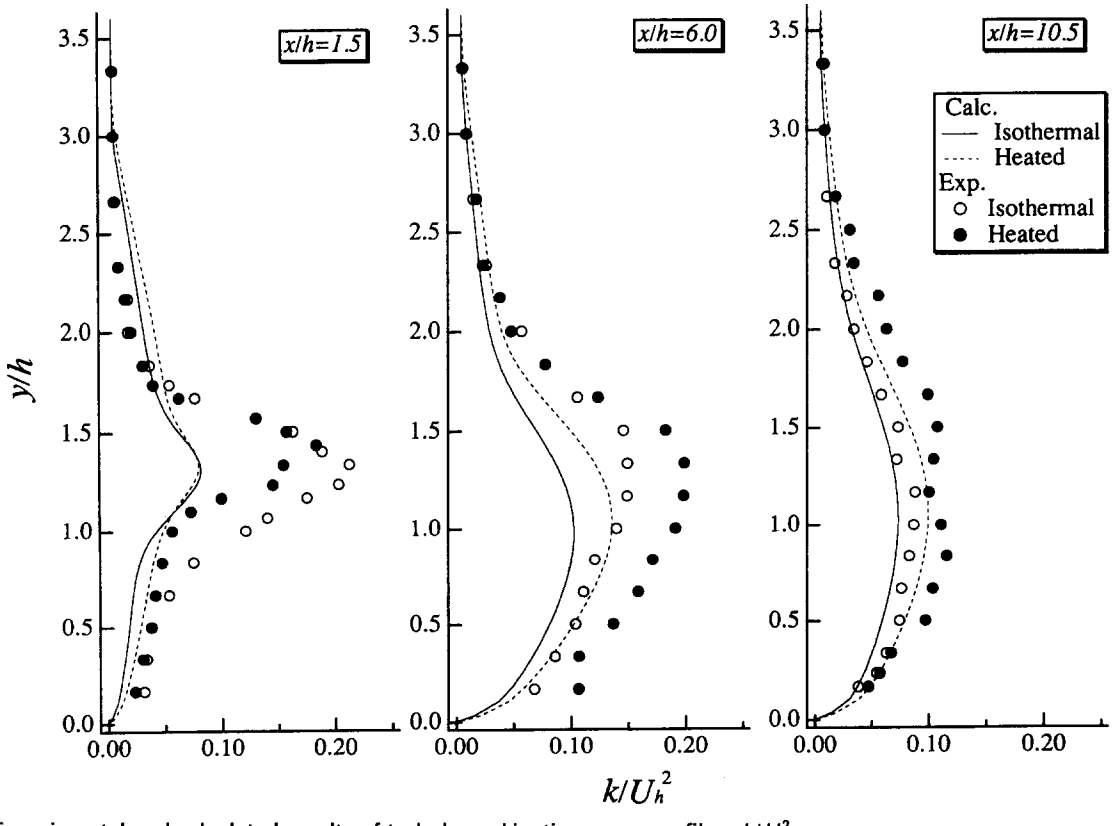

Figure 9 Experimental and calculated results of turbulence kinetic energy profiles, k/U_h^2

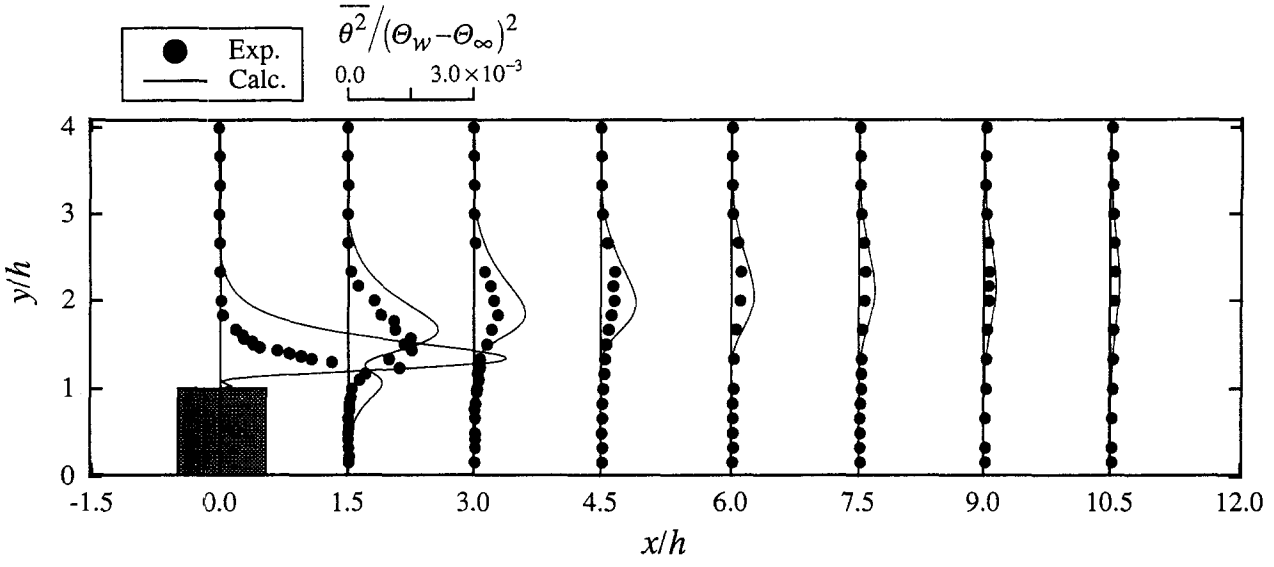

Figure 10 Experimental and calculated results of temperature variance profiles, $\overline{\theta^2}/(\Theta_w - \Theta_\infty)^2$

Further characteristics were obtained from the calculated streamlines. The calculated streamlines for both the isothermal and the heated conditions are presented in Figure 6a and b. The predicted reattachment lengths Xr are $7.0h$ for isothermal condition and $8.4h$ for heated condition. Seeing the streamlines, the heated results in Figure 6b indicate that the dividing streamline ($\rho\psi/\rho_\infty U_h h = 0$) is uplifted over the obstacle head higher than that of isothermal one and keeps a flat curvature further downstream. Qualitatively, the characteristics of the modified mean velocity field due to buoyancy, such as the extension of recirculating region, are clearly observed in the calculated results as well.

The calculated mean temperature profiles were compared with experimental results in Figure 7, showing good agreement qualitatively. The region of the high mean temperature formed near the heat source, especially along the separated shear flow from $x/h = 0$ to 1.5, is considered to act as an effective buoyant motion on the mean velocity field and prevents the separated

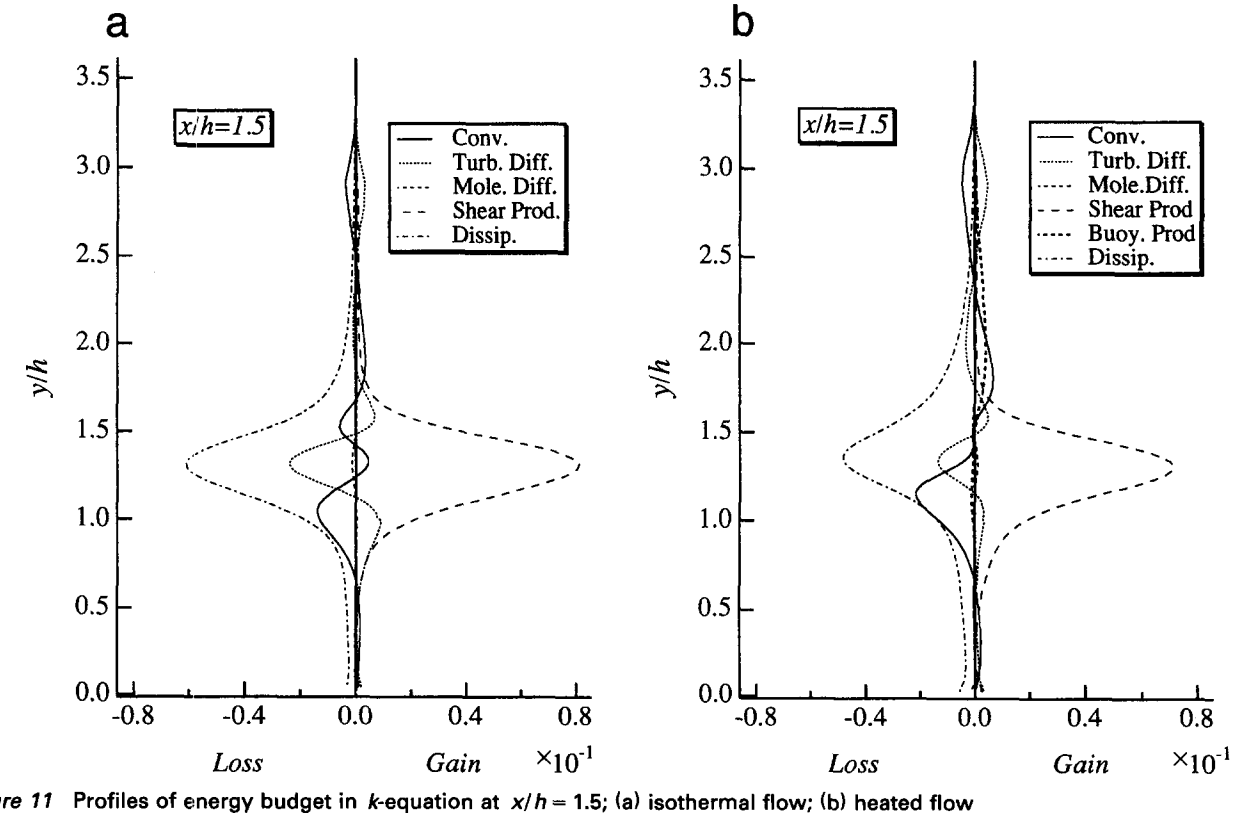

Figure 11 Profiles of energy budget in k-equation at $x/h = 1.5$; (a) isothermal flow; (b) heated flow

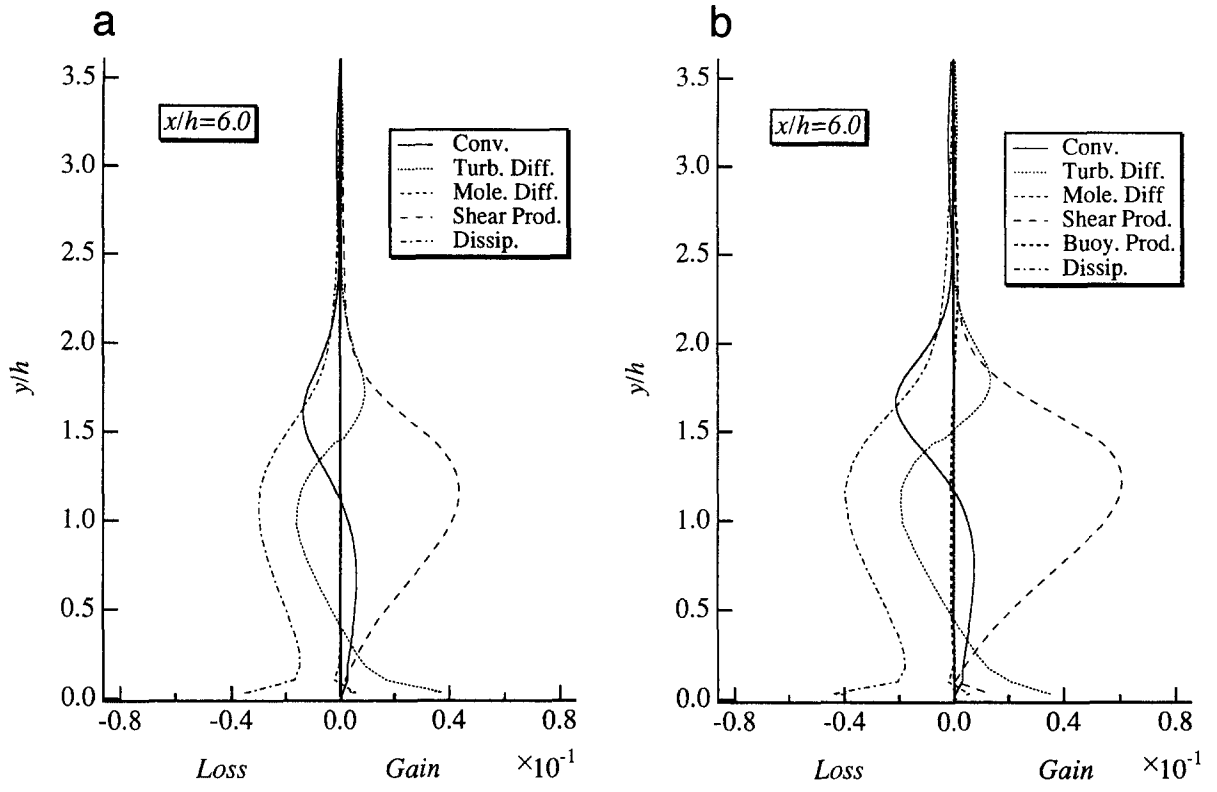

Figure 12 Profiles of energy budget in k-equation at $x/h = 6.0$; (a) isothermal flow; (b) heated flow

shear flow from descending downward. It is also observed in Figure 7 that a negative temperature gradient, so called unstable condition, exists along the outer region of the dividing streamline and the thermal diffusion may mainly occur outside the recirculating region, which results in the significant values of the temperature variance acting as a source of turbulence kinetic energy as described in the later section.

Buoyancy effects on turbulence kinetic energy

Because only $\overline{u^2}$ and $\overline{v^2}$ are measured, the spanwise component $\overline{w^2}$ is approximated as $\overline{w^2} \cong 1/2(\overline{u^2} + \overline{v^2})$, which is the typical treatment for parabolic shear layers, so that the turbulence kinetic energy k was defined as $k \cong 3/4(\overline{u^2} + \overline{v^2})$. Experimental results of turbulence kinetic energy profiles are shown in Figure 8. Comparing with the isothermal results, the peak values of k in the heated results were decreased at $x/h = 0$ just over the obstacle head and at $x/h = 1.5$ in the range of $y/h = 0.8$ to 1.3, and also the peak position at $x/h = 1.5$ was uplifted from $y/h = 1.3$ to 1.5. Downstream, larger values for the heated condition are observed from $x/h = 6.0$ to 10.5. The predicted profiles of turbulence kinetic energy at several locations are compared with the experimental data in Figure 9. In the predicted results, there are some quantitative discrepancies as seen particularly in the lower peak values of k at $x/h = 1.5$ and 6.0 than those of experiments. In general, the separated shear flow passing over the obstacle is strongly flapped, with the time dependency of the separated shear flow being unsteady. So that the values in the k-profiles obtained from the experiment can be gained by this implicit state of separated shear flow, which cannot be detected by the one-point correlation model derived from the Reynolds-average sense. However, the important points here are that the same qualitative trends of overall feature observed in the experimental results, such as the decrease of the peak value of k at $x/h = 1.5$ and the increase further downstream from $x/h = 6.0$ to 10.5, are well obtained in the predictions.

The calculated temperature variance, an important agent of the buoyant production G_k in the k-equation, is compared with the measurement in Figure 10. The peak positions in the calculated profiles in Figure 10 are coincident with those of experiment downstream, but the calculated values are wholly overpredicted for the reason arising from the overprediction of mean temperature gradient as previously shown in Figure 7. The temperature variance is produced by the interaction between the mean temperature gradient and the turbulent heat flux; therefore, the profiles of the temperature variance are spread in accordance with the mean temperature gradient $\partial\Theta/\partial y$.

The buoyancy effects in the k-profile can be deduced from the difference of the turbulence energy budget between the isothermal and the heated conditions. Although we have only calculated results of the budget profile, the qualitative comparison is possible to clarify what are observed in the turbulence kinetic energy profiles. The comparisons of calculated budgets at $x/h = 1.5$ and 6.0 are presented respectively in Figures 11 and 12, for isothermal and heated conditions (normalized by $\rho_\infty U_h^3/h$). In the case of the heated flow at $x/h = 1.5$ in Figure 11b, the contribution of the shear production term to the gain factor is decreased extensively, with a peak reduction of nearly 10%. It is also shown in Figure 11b that the contribution of the convection term to the loss factor is slightly increased in the range of $0.6 < y/h < 1.3$, which corresponds to the gained negative mean velocity due to the expansion of the recirculating region. The former factor, the modified shear production term, appears to be mainly attributed to the reduction of the peak value in the turbulence kinetic energy profile at $x/h = 1.5$. Also at $x/h = 1.5$ in Figure 11b, the buoyant production acts as a source in the range of $1.5 < y/h < 2.5$ where the shear production is absent, but the buoyant production is not evident in the experimental results of k in this region, as shown in Figure 8. Seeing the calculated budgets at $x/h = 6$ in Figures 12a and 12b, the buoyant contribution has almost disappeared, and the much larger value of the

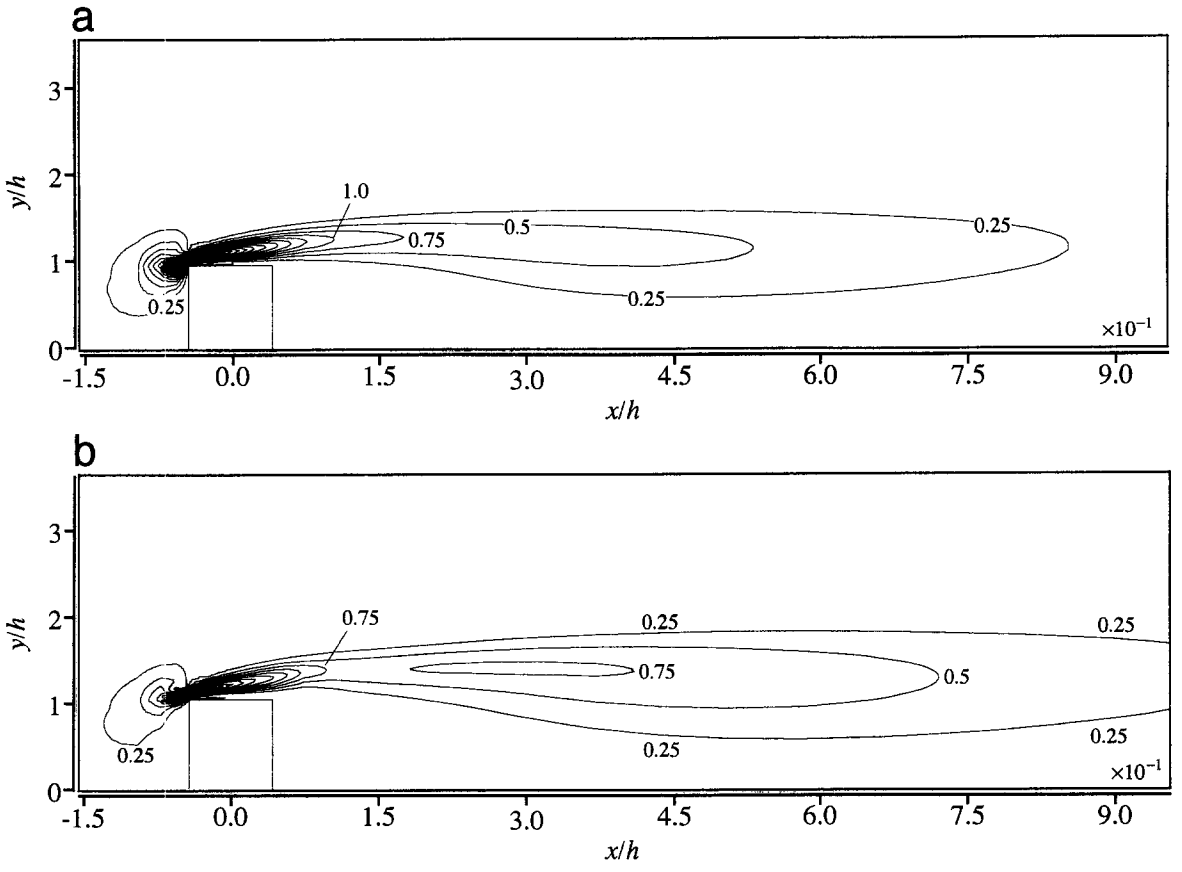

Figure 13 Calculated contours of shear production term, $P_k/(\rho_\infty U_h^3/h)$; (a) isothermal flow; (b) heated flow

shear production term appears in the gain factor, which dominates the source of turbulence kinetic energy. Also in Figure 12b, the negative contribution of the energy dissipation is increased in accordance with the larger profile of shear production term. Accordingly, the cause of what is observed in the k-profiles under the buoyancy effects can be principally attributed to the modification of the shear production term through the altered mean velocity field.

The calculated contours of the shear production term P_k are presented in Figures 13a and 13b for isothermal and heated conditions, each of which obviously shows the notable difference in P_k distribution. In Figure 13a, P_k of the isothermal flow declines from the obstacle downstream, while P_k of the heated flow in Figure 13b decreases rapidly from $x/h = 0$ to $x/h = 1.5$, and then the peak value increases again between $x/h = 1.5$ and 4.5.

Finally, the predicted contour of flux Richardson number $R_f = -G_k/P_k$, a ratio of buoyant production to shear production of turbulence kinetic energy, is presented in Figure 14. It is clear that the buoyant production G_k dominates the shear production P_k immediately above the obstacle head and downstream above the recirculating region, which arises from the significant value of the temperature variance produced by the effective mean temperature gradient.

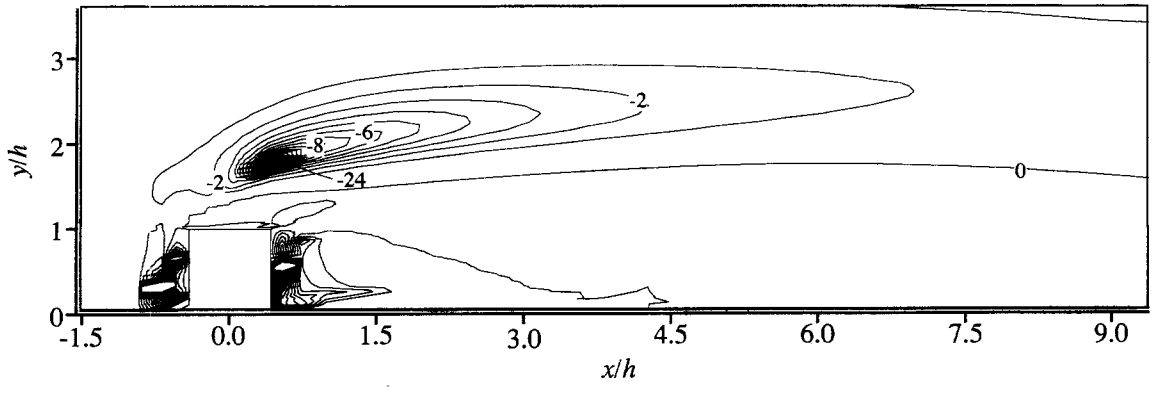

Figure 14 Calculated contours of flux Richardson number, $R_f = -G_k/P_k$

Conclusions

In the present work, the flow characteristics behind a 2-D heated obstacle placed in a turbulent boundary layer was investigated both experimentally and numerically to clarify the effects of buoyancy on the fluid motion in which complex topography and thermal release were incorporated. In particular, the greatest attention was given to the modification of the production agencies of the turbulence kinetic energy. A k-ε model was used with the algebraic flux model for buoyant extension (Launder 1989) and gave predictions that roughly agreed with the experimental results. However, it clarified certain features of the buoyancy on the wake qualitatively. The comparison of the results between isothermal and heated conditions established the following particular conclusions;

(1) The thermal accumulation behind the obstacle changes the mean flow in the wake. The buoyancy effects on the mean velocity field is observed mainly in the recirculating region.
(2) As a result of the modified shear profile by buoyancy, the turbulence kinetic energy is reduced in the vicinity of the obstacle and increased downstream.
(3) Direct buoyant production does not appear to affect the turbulence energy profile in the wake. However, in the region external to the recirculating zone, where the effective mean velocity gradient is absent, the buoyant production dominates the shear production because of the finite values of the temperature variance created by the mean temperature gradient. Therefore, the noncoincidence of the mean velocity and temperature gradient in the flow is responsible for the difference in the relative magnitudes of the production terms of turbulence kinetic energy.

Acknowledgments

The authors gratefully thank Mr. Y. Tawaraya, a graduate student at Keio university, for his enthusiastic assistance in conducting the experiment. We also thank to Dr. Epaminondas Mastorakos (IFP/France) for his valuable comments concerning the previous work.

References

Béguier, C., Dekeyser, I. and Launder, B. E. 1978. Ratio of scalar and velocity dissipation time scales in shear flow turbulence. *Phys. Fluids*, **21**, 307–310

Corrsin, S. 1951. The decay of isotropic temperature fluctuations in an isotropic turbulence. *J. Aeronaut. Sci.*, **18**, 417–423

Davidson, L. 1990. Calculation of the turbulent buoyancy-driven flow in a rectangular cavity using an efficient solver and two different low Reynolds number k-ε turbulence models. *Num. Heat Transfer*, Part A, **18**, 129–147

Demuren, A. O. and Rodi, W. 1987. Three-dimensional numerical calculations of flow and plume spreading past cooling towers. *ASME J. Heat Transfer*, **109**, 113–119

Gibson, M. M. and Launder, B. E. 1978. Ground effects on pressure fluctuations in the atmospheric boundary layer. *J. Fluid Mech.*, **86**, 491–511

Hanjalić, K. and Vasić, S. 1993. Computation of turbulent natural convection in rectangular enclosures with an algebraic flux model. *Int. J. Heat Mass Transfer*, **36**, 3603–3624

Khosla, P. K. and Rubin, S. G. A. 1974. Diagonally dominant second-order accurate implicit scheme. *Computers & Fluids*, **2**, 207

Kato, M. and Launder, B. E. 1993. The modeling of turbulent flow around stationary and vibrating square cylinders. *Proc. 9th Symposium on Turbulent Shear Flows*, Kyoto, Japan

Launder, B. E. 1975. On the effects of a gravitational field on the turbulent transport of heat and momentum. *J. Fluid Mech.*, **67**, 569–581

Launder, B. E. 1989. On the computation of convective heat transfer in complex turbulent flows. *ASME J. Heat Transfer*, **110**, 1112–1128

Markatos N. C., Malin, N. R. and Cox, G. 1982. Mathematical modeling of buoyancy-induced smoke flow in enclosures. *Int. J. Heat Mass Transfer*, **25**, 63–75

Obi, S. and Perić, M. A. 1991. Co-located finite-volume method for non-orthogonal grid with a second-moment turbulence closure. *Proc. 4th Internation Symposium CFD*, Davis, CA

Obi, S. 1991. Berechnung Komplexer Turbulenter strömungen mit einem Reynolds-spannungs-modell. Ph.D. Thesis, Erlangen, Germany

Perić, M. and Scheuerer, G. 1989. CAST — A Finite volume method for predicting two-dimensional flow and heat transfer phenomena. Gesellschaft für Reaktorsicherheit (GRS), Technical Note SRR-89-01.

Tennekes, H. and Lumley, J. L. 1973. *A First Course in Turbulence*. Massachusetts Institute of Technology Press, Cambridge, MA

Turner, J. S. 1973. *Buoyancy Effects in Fluids*. Cambridge University Press, Cambridge, UK

Viollet, P. L. 1987. The modelling of turbulent flows for the purpose of reactor thermal-hydraulic analysis. *Nucl. Eng. Design*, **99**, 365–377